Experiments in Fluids 30 (2001) 93–101 © Springer-Verlag 2001

Simultaneous imaging of temperature and mole fraction using acetone planar laser-induced fluorescence

M. C. Thurber, R. K. Hanson

Abstract Imaging of concentration with acetone PLIF has become popular in mixing investigations. More recently, studies of the temperature dependences of acetone fluorescence have enabled quantitative imaging of temperature using single- or dual-wavelength excitation strategies. We present here the first demonstration of simultaneous imaging of temperature and mole fraction with acetone PLIF. Laser excitation is at 248 and 308 nm; the resulting fluorescence images are captured by an interline transfer CCD camera capable of acquiring two frames with a separation in time of as little as 500 ns. In addition to adding temperature imaging capability, this dual-wavelength approach enables mole fraction to be accurately measured in non-isothermal flows. Tests in a heated turbulent jet demonstrate the ability to record instantaneous mole fraction and temperature structure. The expected correspondence of the temperature and concentration fields is observed, and mean values of these quantities derived from image averaging show the expected radial and centerline profiles as the jet becomes fully developed.

1 Introduction

The relatively straightforward application and interpretation of imaging diagnostics based on planar laser-induced fluorescence (PLIF) of acetone have made such diagnostics popular in gas-phase studies of mixing (Lozano 1992; Yip et al. 1994; Smith and Mungal 1998), in which acetone is seeded into a flow as a quantitative indicator of concentration (mole fraction or number density). Acetone has been applied as a fuel marker in diffusion flames (Clemens and Paul 1995) and internal combustion engines (Wolff et al. 1993), although uncertainties regarding the temperature dependence of acetone fluorescence have in the past complicated efforts to make quantitative measurements in non-isothermal environments. More recently, improved understanding of the temperature and excitation wavelength dependences of acetone fluorescence (Tait and Greenhalgh 1992; Grossmann et al. 1996; Ghandhi and Felton 1996; Bryant et al. 1997; Thurber et al. 1998) has furthered the development of quantitative concentration diagnostics for non-isothermal flowfields, while allowing for the first time the demonstration of quantitative temperature imaging with acetone PLIF in atmospheric-pressure flows.

Single- and dual-wavelength temperature imaging techniques have been demonstrated (Thurber et al. 1997), with the former suitable in flows with uniform acetone partial pressure and the latter required where pressure or acetone seeding vary across a flowfield, e.g., in cases of mixing or chemical reaction. The single-wavelength technique has shown good temperature sensitivity examining flow over a heated cylinder with 248 nm excitation, as well as the ability to capture instantaneous temperature structure in a uniformly seeded transverse jet flowfield with 266 nm excitation (Thurber et al. 1998). Dual-wavelength measurements, which ratio fluorescence images from laser excitation at two different wavelengths, require either a steady flow, as in a previous demonstration case of a heated laminar jet mixing with ambient air, or the ability to record fluorescence images on a near-simultaneous basis. The latter approach is preferred, as many flows of practical interest are turbulent.

The acquisition of two near-simultaneous fluorescence images can, in fact, provide dual-parameter imaging capability (Thurber et al. 1998), yielding either concentration (uniform-pressure flow) or pressure (uniform acetone seeding) in addition to temperature. In the combined temperature/mole fraction measurement approach that will be considered here, the image of temperature derived from the dual-wavelength technique allows compensation of a single of the two fluorescence images for temperature variation so that an image proportional to the mole fraction is produced. The ability to generate instantaneous maps of mole fraction and temperature holds promise for the study of flows characterized by mixing, unsteadiness, temperature variation, and chemical reaction.

The emerging capabilities of interline transfer CCD cameras, demonstrated to be effective in particle imaging velocimetry (PIV) studies, are also ideally matched to a dual-image fluorescence technique, allowing the acquisi-

Received: *13 January 1999/Accepted 10 February 2000*

M. C. Thurber (✉), R. K. Hanson
High Temperature Gasdynamics Laboratory
Department of Mechanical Engineering
Stanford University, Stanford, CA 94305-3032, USA

This research was sponsored by the US Air Force Office of Scientific Research, Aerospace and Materials Sciences Directorate, with Dr. J. Tishkoff as the technical monitor. In addition, the authors would like to acknowledge the assistance of L. Muñiz, E. F. Hasselbrink, L. Su, and B. J. Kirby.

tion of two images in rapid (~500 ns) succession with little increase in experimental complexity. We apply this type of camera to record instantaneous images of temperature and mole fraction in a heated, turbulent jet with weak coflow. Comparison of ensemble-averaged image results to each other and to turbulent jet correlations allows quantitative evaluation of the technique.

2 Theory of acetone PLIF

2.1 Acetone fluorescence properties

The fluorescence properties of acetone make it well-suited for use as a PLIF tracer. Its broadband absorption feature (225–320 nm) is accessible with high-pulse-energy UV lasers, and the non-resonant visible fluorescence (350–550 nm) can be collected with low-noise, unintensified CCD cameras. Laser-induced fluorescence occurs from the first excited singlet state S_1, with a fluorescence quantum yield limited by rapid intersystem crossing from S_1 to the first excited triplet T_1. The essentially intramolecular nature of this de-excitation process, in contrast to the collisional quenching that limits fluorescence for important diatomic tracers such as OH and NO, results in comparatively minor, though not always negligible, dependences of fluorescence on pressure and composition. In the past, therefore, the fluorescence yield of acetone has frequently been modeled as a constant, though more accurate recent models (Yuen et al. 1997; Thurber et al. 1998) incorporate pressure, composition, wavelength, and temperature dependences due to the competition between vibrational relaxation and non-radiative electronic de-excitation of excited singlet acetone.

For weak excitation, the overall fluorescence signal from acetone is given by:

$$S_f = \frac{E}{hc/\lambda}\eta_{opt}\, dV_c\left[\frac{\chi_{acetone}P}{kT}\right]\sigma(\lambda,T)\phi\left(\lambda,T,P,\sum_i \chi_i\right) \quad (1)$$

Here, E is the laser fluence (J/cm^2), (hc/λ) is the energy (J) of a photon at the excitation wavelength λ, η_{opt} is the overall efficiency of the collection optics, and dV_c is the collection volume (cm^3). The bracketed term is the acetone number density (cm^{-3}), given as the product of mole fraction $\chi_{acetone}$ and total pressure P divided by the Boltzmann constant k times temperature T. The final two quantities are σ, the molecular absorption cross-section of the tracer (cm^2), and ϕ, the fluorescence quantum yield.

2.2 Concentration and temperature measurement strategies

Considering only terms in the fluorescence equation that are dependent on properties of the gas mixture, and neglecting the effect of composition variation on fluorescence yield, we find:

$$S_f \propto \left[\frac{\chi_{acetone}P}{kT}\right]\sigma(\lambda,T)\phi(\lambda,T,P) \quad (2)$$

For a given excitation wavelength and conditions that are isothermal and isobaric, the fluorescence signal is proportional to the number density or mole fraction. For constant-pressure flows with temperature variation, understanding of the variation in σ and ϕ with temperature and excitation wavelength is required for quantitative measurement of number density or mole fraction using fluorescence. Equation (2) also suggests several approaches to imaging temperature.

First, at conditions of uniform seeding and total pressure, a single-wavelength excitation strategy is possible. Denoting S_f^+ the fluorescence signal per unit acetone mole fraction at constant pressure, we see that:

$$S_f^+ \propto \frac{1}{T}\sigma(\lambda,T)\phi(\lambda,T,P) \quad (3)$$

If the temperature dependence of the right-hand side of Eq. (3) has been determined for excitation wavelength λ and total pressure P, measurement of fluorescence in conjunction with a single calibration point in the flow provides an indication of temperature. The pressure dependence of the fluorescence yield may be sufficiently weak that the temperature dependence of ϕ determined at a calibration pressure is suitable for use at nearby pressures as well (Thurber et al. 1998; Thurber and Hanson 1999).

In the less restrictive case in which acetone partial pressure may vary across the flow, temperature measurements can be obtained using a dual-excitation-wavelength approach. As shown in Eq. (4), number density cancels in the ratio of fluorescence signals resulting from excitation at different wavelengths.

$$\frac{S_{f,\lambda_2}}{S_{f,\lambda_1}} = \frac{\sigma(\lambda_2,T)\phi(\lambda_2,T,P)}{\sigma(\lambda_1,T)\phi(\lambda_1,T,P)} \quad (4)$$

If the right-hand side of Eq. (4) is a known function of temperature for the given excitation wavelengths and a pressure sufficiently close to that encountered in the flow, the fluorescence ratio measurement, again with a single temperature calibration point, yields temperature data. Temperature measurement with the dual-wavelength technique at the same time enables quantitative measurement of concentration in cases where temperature variation previously precluded this possibility.

2.3 Measured temperature dependences for diagnostics

Experimental measurements of the temperature dependences of fluorescence from acetone dilute in nitrogen at atmospheric pressure, the details of which are described separately (Thurber et al. 1998), allow selection of optimal excitation wavelengths for both concentration and temperature diagnostics. Figure 1a plots S_f^+, the fluorescence signal per unit mole fraction, as a function of temperature for five excitation wavelengths across the acetone absorption feature. A mole fraction diagnostic is seen to function best with use of a longer wavelength (for example, XeCl excimer laser output at 308 nm) for minimum temperature dependence. A single-wavelength temperature measurement, on the other hand, should use excitation at 248 or 266 nm, as both wavelengths show steep changes in

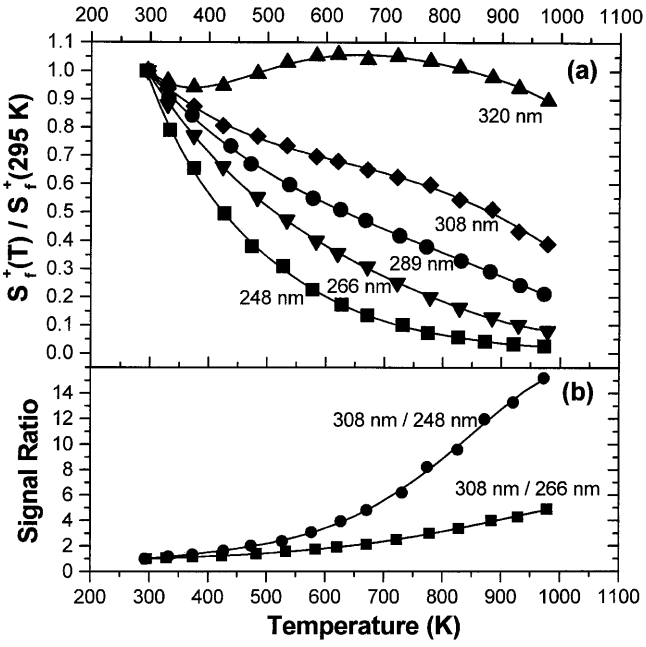

Fig. 1. **a** Plots of S_f^+ (fluorescence per unit acetone mole fraction) with temperature at $P = 1$ atm, normalized to the room temperature value for each excitation wavelength. **b** Temperature behavior of the fluorescence ratio, generated by dividing one curve of S_f^+ by another

fluorescence with temperature and can be generated with high-pulse-energy UV lasers.

For diagnostic applications in which single-wavelength temperature imaging is not possible, Fig. 1b shows the temperature dependences of fluorescence signal ratios obtained from excitation with either 308- and 248-nm or 308- and 266-nm wavelength pairs. The 308/248-nm line pair shows highest inherent sensitivity to temperature. A simultaneous measurement of temperature and mole fraction in a flow of interest can use the 308/248-nm fluorescence ratio to generate a temperature map of the flow, and then apply this known temperature field to correct the 308-nm image according to the temperature dependence in Fig. 1a, so that the resulting image is proportional to the mole fraction.

Table 1 displays in tabular form the fluorescence data plotted in Fig. 1a. As in the figure, the fluorescence signal is normalized to the room temperature value for each excitation wavelength and given on a per unit acetone mole fraction basis. In experimental application of a single- or dual-wavelength temperature diagnostic, the fluorescence signal or fluorescence signal ratio values derived from Table 1 are fit to temperature over the temperature range in question. With a known calibration point, this fit allows the fluorescence image (single-wavelength technique) or image ratio (dual-wavelength technique) to be converted to temperature.

2.4
Consideration of pressure and composition effects

The flow considered in the current work is at the same atmospheric-pressure condition at which the temperature-dependence data of Fig. 1 was acquired. An air bath gas replaces the nitrogen used in the temperature-dependence data, a substitution which experiments described separately (Thurber and Hanson 1999) have shown to have no significant effect on acetone fluorescence at atmospheric pressure and room temperature. It was additionally verified as part of the current work that there is no detectable difference between acetone fluorescence with air and with nitrogen bath gases at temperatures up to 600 K (the highest achievable with the heated jet arrangement employed). A useful feature of an air bath gas is that it completely quenches acetone phosphorescence, obviating the need for a gated camera for fluorescence collection.

For a hypothetical experiment significantly removed from the atmospheric-pressure acetone/nitrogen datum condition, consideration of pressure and composition effects may be necessary, though as a general rule these effects remain weak compared with the case of tracers with strong collisional quenching of fluorescence. In acetone, pressure and composition influences on fluorescence yield arise from the competition between vibrational relaxation and vibrational-energy-dependent electronic relaxation (intersystem crossing or dissociation) of molecules in the excited singlet manifold. Increases in pressure or in the effectiveness of collision partners at relaxing acetone will result in excited acetone molecules being more rapidly

Table 1. Normilized S_f^+ with temperature at $P = 1$ atm and different excitation wavelengths

T_{248} [K]	S_{248}^+	T_{266} [K]	S_{266}^+	T_{289} [K]	S_{289}^+	T_{308} [K]	S_{308}^+	T_{320} [K]	S_{320}^+
293	1.000	296	1.000	296	1.000	296	1.000	293	1.000
333	0.789	329	0.880	331	0.906	330	0.938	323	0.963
374	0.654	374	0.770	371	0.842	374	0.875	370	0.942
427	0.495	424	0.660	437	0.734	424	0.806	422	0.948
474	0.380	483	0.552	472	0.670	483	0.769	474	0.990
527	0.310	533	0.473	538	0.597	533	0.735	532	1.030
577	0.226	584	0.399	578	0.550	584	0.697	573	1.052
627	0.173	620	0.356	625	0.510	620	0.680	621	1.058
671	0.135	671	0.309	668	0.472	680	0.650	670	1.040
731	0.101	722	0.251	726	0.418	722	0.624	725	1.051
774	0.073	778	0.200	772	0.380	778	0.598	774	1.035
826	0.057	828	0.162	831	0.330	828	0.545	834	1.012
872	0.043	884	0.128	881	0.292	884	0.511	876	0.978
921	0.033	929	0.102	932	0.243	929	0.433	926	0.941
973	0.026	978	0.080	973	0.212	978	0.389	976	0.896

returned to the ground vibrational state of the excited singlet manifold. Since the electronic relaxation rate that limits fluorescence yield is an increasing function of vibrational energy, this quicker vibrational relaxation has the effect of increasing the overall fluorescence yield. Increases in temperature or laser excitation energy, associated with acetone molecules' being placed in higher-lying initial vibrational levels of the excited singlet, will result in greater exposure to higher electronic de-excitation rates, and therefore lower fluorescence yields. Relative pressure and composition effects are weakest at low excitation energies (long wavelengths), for which the initially excited vibrational states are lowest in energy, and strongest at high excitation energies (short wavelengths).

The effects on fluorescence yield predicted by the model for variations in pressure, temperature, and excitation wavelength have been observed in several studies (Grossmann et al. 1996; Ossler and Aldén 1997; Yuen et al. 1997; Thurber and Hanson 1999). Composition effects can also be treated with the model. In general, size of collision partner is roughly correlated with effectiveness at relaxing vibrationally excited polyatomics (Rossi et al. 1983; Hippler et al. 1989), so an increase in acetone fluorescence yield with increasing complexity of collision partner is expected. Experiments confirm this behavior (Thurber and Hanson 1999). An effect that requires separate explanation is the reduction in fluorescence intensity observed in the presence of high partial pressures of oxygen (Grossmann et al. 1996; Ossler and Aldén 1997; Yuen et al. 1997; Thurber and Hanson 1999); this is hypothesized to result from an intersystem crossing process that is enhanced by the presence of naturally occurring ground-state oxygen triplets. For an air bath gas, this oxygen effect first becomes significant at a total pressure of several atmospheres, with roughly 10% reduction in fluorescence of acetone in air compared with nitrogen by 4 atm (Thurber and Hanson 1999). For a pure oxygen bath gas, the effect is already important at 1 atm, in agreement with a simple understanding of the assisted intersystem crossing process in which the controlling rate is proportional to oxygen number density. Although the temperature dependence of this process is not well understood, experimental results are fit reasonably well with the assumption of negligible temperature dependence.

A quantitative model of fluorescence yield that incorporates the above effects of pressure, composition, temperature, and excitation wavelength has been shown to match reported experimental data acceptably well (Thurber et al. 1998; Thurber and Hanson 1999). This success suggests that the model can be used to improve the accuracy of diagnostic applications at conditions – for example, pressures other than 1 atm – at which direct temperature-dependence information is not available. A particularly useful application of the model is to account for the variation in composition between two streams that are mixing in a flowfield. In the experiments described here, for instance, an air coflow stream with low acetone seeding mixes with a heated air jet with higher acetone seeding. Because acetone–acetone vibrational relaxation is significantly more efficient than acetone–air relaxation, even small variations in acetone seeding can have a detectable effect on mixture fluorescence yield. At room temperature and atmospheric pressure, the ratio of fluorescence yields from 308 and 248 nm excitation varies about 9% between air streams seeded with 1 and 22% acetone, which would result in noticeable error in the temperature derived from the fluorescence ratio. Applying the knowledge of composition dependences derived from model and experiment allows an initial acetone mole fraction image acquired in a dual-wavelength diagnostic application to be used to correct for this effect of composition on fluorescence yield. Such a procedure can be followed for the mixing of streams with different acetone mole fractions even when the bath gases are dissimilar, as in the case of acetone-seeded fuel mixing with unseeded oxidizer. Calibration experiments may be required if the relative effectiveness of a particular gas mixture at relaxing vibrationally excited acetone is not known a priori.

3 Experimental approach

Simultaneous temperature/mole fraction imaging of a heated turbulent jet in weak coflow (Fig. 2) provides a diagnostic validation case for which averaged results can

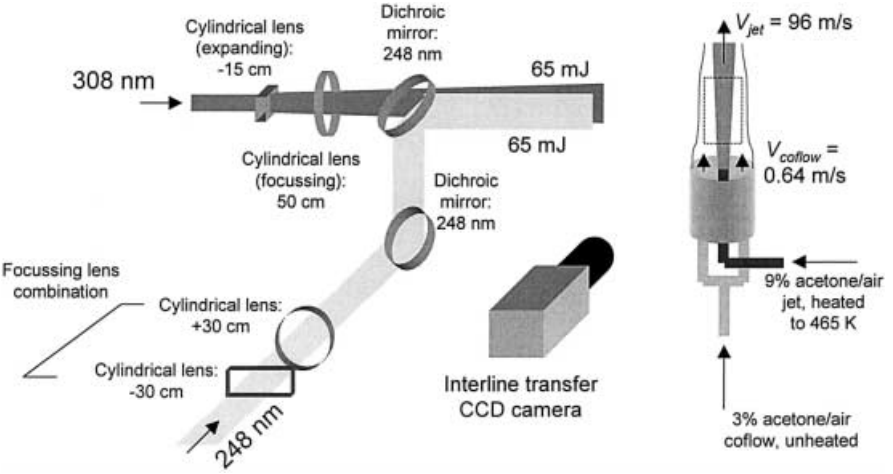

Fig. 2. Experimental schematic

be compared against correlations, and instantaneous images can test the ability to resolve fine structure. Seeding jet and coflow with differing amounts of acetone allows measurement of temperature and mixture fraction throughout the flowfield. The room temperature coflow, seeded weakly with a uniform concentration of acetone, provides for both temperature calibration and laser sheet intensity compensation. Laser sheets at 248 and 308 nm are aligned to be precisely coplanar and passed through the jet centerline with 800 ns temporal separation. The resulting fluorescence images are successively captured onto the array of a single interline transfer CCD camera with dual-image acquisition capability.

The specific flow considered is a 96 m/s turbulent jet (Re = 5,100) of acetone-seeded air emanating from the 1.7-mm nozzle exit of an electrical air heater (Sylvania 014683), with an exit temperature of $T_j = 465$ K. The nozzle is a 30:1 conical contraction with 9° half-angle. The Froude number of the resulting jet is quite high ($\sim 1 \times 10^6$), indicating negligible effects of buoyancy in the region of the jet considered (from the nozzle extending 21 diameters downstream). A 0.64 m/s acetone/air coflow at room temperature issues from a surrounding tube with a 5-cm inner diameter. The jet and coflow are seeded to approximately 9% and 3% acetone, respectively, by bubbling the air streams through liquid acetone and adding additional dilution air to the coflow.

Laser sheets at 248 and 308 nm, generated by KrF and XeCl excimers, respectively, pass through the jet centerline just above the nozzle; the 308 nm sheet is delayed 800 ns relative to the 248 nm sheet. Each sheet consists of approximately 65 mJ focused to a waist 40 mm high and 0.5 mm across. For the dual-wavelength technique to work effectively, identical packets of fluid must be captured in the respective laser sheets. The fine scales of turbulent structure in this flowfield therefore make sheet focusing and alignment particularly important. To permit independent control of each sheet, separate focusing branches are employed in the optical layout (Fig. 2), with the two sheets then combined by a dichroic mirror. It is found that the two sheets can be effectively aligned relative to each other by examining the images off of a weakly fluorescing material – for example, a block of aluminum – placed on the jet centerline at an oblique angle to the incoming beams.

Acetone fluorescence excited by each laser sheet is captured in turn onto the array of an interline transfer CCD camera that has the ability to acquire and store two images in swift succession (Princeton Instruments MicroMax RTE/CCD-1300Y with Double Image Feature). Charge accumulated from the first fluorescence pulse is rapidly shifted under a masked portion of the CCD array, allowing acquisition of the second frame to begin immediately on the photosensitive portion of the array. Readout of the two stored images occurs more slowly, in 1.4 s per image for the full 1,300 × 1,030 array. This type of camera provides the capability of acquiring two images with identical collection optics and an intervening interval as short as 400 ns, limited by the time required to transfer the charge on each pixel under the mask. Since acquisition of the first frame is ended by this rapid charge transfer, the first frame exposure time subsequent to the fluorescence pulse can be as short as several hundred nanoseconds. Minimum exposure of the second frame, limited by an internal mechanical shutter, is on the order of 8 ms.

Other performance characteristics of the camera are suited to an acetone dual-wavelength fluorescence experiment as well. Quantum efficiency (including the effects of on-chip microlenses) peaks at 50% at 400 nm, near the acetone fluorescence peak at 430 nm. A low system noise floor of 6–9 electrons allows realization of a dynamic range of 11 bits or better (digitization is to 12 bits), which is necessary to accommodate the large variation in fluorescence signal in experiments covering a wide temperature range.

Using a 50-mm focal length, *f*/1.2 lens with an 8-mm extension tube, a region of the flow 33 mm by 42 mm in size is imaged at 1:5 magnification onto the CCD array. To improve the signal-to-noise ratio of the fluorescence images, the 6.7-μm-square pixels on the array are binned 2 × 2 into larger 13.4-μm pixels, each of which corresponds to a physical region in the flow 64 μm on a side. At the highest velocity encountered in the flow, 96 m/s in the jet potential core, a fluid element will move 77 μm in the 800 ns between fluorescence pulses, just slightly more than the binned pixel dimension. While minor pixel-to-pixel blurring of jet structure may therefore occur in the 308/248-nm ratio image on the jet centerline near the nozzle exit, this comparison suggests that, in general, the temperature/mole fraction diagnostic provides flow-stopping temporal resolution throughout the flowfield, especially given the rapid radial and centerline decay of velocity due to turbulent mixing. The total duration of the fluorescence pulse itself – less than 30 ns, limited by the laser pulse duration – is significantly shorter than any fluid time scales of importance.

Conversion of the fluorescence images to temperature and concentration is facilitated by the presence of a room-temperature, acetone-seeded coflow. Following background subtraction, a cut along the coflow before the jet in each of the two fluorescence image frames provides a measure of the sheet energy distribution for both the 248-nm excitation (first frame) and the 308-nm excitation (second frame). Using this information along with measurements of the sheet divergence and shift for each wavelength, we separately correct the instantaneous 248- and 308-nm fluorescence images for variations in sheet energy in space and time. This correction also approximately accounts for variations in optical collection efficiency in the jet axial direction. (In a prior step, the small variations in optical collection efficiency radially across the jet were corrected for by dividing by an additional image obtained with a uniform flow of acetone filling the field of view, itself suitably corrected for absorption and laser sheet intensity variation.)

The ratio of the sheet-corrected fluorescence images from 308- and 248-nm excitation, respectively, then provides an indication of temperature as in Fig. 1. To perform the conversion to temperature, the image processing routines use curve fits to the ϕ–T data of Table 1 over an appropriate range – in this case, 297–630 K – to generate a look-up table relating signal ratio to temperature. The signal ratio image is multiplied by a suitable constant to yield the correct coflow temperature of 297 K. The result-

ing temperature image is in turn used to convert the 308-nm fluorescence image to a map of mole fraction using another look-up table describing the variation in 308-nm signal with temperature at constant acetone mole fraction.

These initial images of mole fraction and temperature, along with information on laser sheet geometry, allow a pixel-by-pixel correction for laser absorption to be performed on the initial fluorescence images. In addition, these fluorescence images can be corrected for the small effect of variable acetone seeding on fluorescence yield by including a description of this effect (Thurber and Hanson 1999) in the processing routine. Following these corrections, the conversion of the ratio image to temperature and the 308-nm image to concentration are repeated to produce the final temperature and mole fraction results. By scaling the coflow mole fraction to 0 and the jet mole fraction to 1, the mole fraction image can be directly converted into molar jet mixture fraction ξ_{jet}, defined as:

$$\xi_{\text{jet}} = \frac{N_{\text{jet}}}{N_{\text{jet}} + N_{\text{coflow}}} \tag{5}$$

where N_{jet} is the number of moles of jet fluid, and N_{coflow} is the number of moles of coflow fluid in an elemental volume in the flow. ξ_{jet} is here expressed as a percentage varying between 0% jet fluid (coflow) and 100% jet fluid (jet potential core).

An important validation of the temperature measurement approach is obtained by verifying that it yields a featureless image of indicated temperature in a uniform-temperature flowfield. Figure 3, picturing three instantaneous "temperature" images of a room-temperature jet in room-temperature coflow, demonstrates the kinds of errors that can arise in a dual-wavelength temperature imaging experiment. For each image in Fig. 3, the turbulent jet is seeded to about 18% acetone while the coflow contains roughly 6%. In the first case (Fig. 3a), the 248 and 308 nm sheets are rotated slightly with respect to each other. The result of this misalignment is dramatic: because slightly different packets of fluid are imaged by the respective sheets, temperature variations of up to ±50 K are erroneously indicated. In the second image (Fig. 3b), the sheet misalignment has been corrected, but correction for the more minor effect of acetone concentration on fluorescence yield has not been performed. As a result, there is still a faint temperature image of the jet showing an indicated jet temperature about 10 K lower than ambient. The higher acetone mole fraction in the jet leads to a slightly higher fluorescence yield there, particularly at 248 nm, which is falsely interpreted by the processing routine as an indication of lower temperature. The third image (Fig. 3c) shows the indicated temperature field when this effect is taken into account as well. The disparity between indicated temperature of jet and ambient essentially disappears, except in a small remaining region of minor sheet misalignment near the jet nozzle.

4
Results and discussion

The turbulent heated jet provides a good diagnostic test case, requiring the ability to capture instantaneous temperature/concentration structure on fine scales, while at the same time providing a reasonably well-characterized average field for comparison with image data. The imaged region examined in these experiments, $x/d = 2$ to $x/d = 21$, extends from the jet potential core just into the fully developed zone in which mean-field quantities can be expected to be self-similar (Chen and Rodi 1980; Dowling and Dimotakis 1990). A detailed study of the fluid mechanics of this particular jet would extend to higher x/d values to allow accurate derivation of jet scaling constants. For purposes of diagnostic validation, however, use of this more limited region is perfectly adequate, providing good spatial resolution, high signal-to-noise ratio throughout the images, and an area within the field of view where similarity behavior can be evaluated. In variable-density jets such as this one, similarity still holds where the local density ratio of ambient to centerline fluid has dropped to near unity, albeit with jet scaling constants modified by the factor of $(\rho_{\text{jet exit}}/\rho_{\text{ambient}})^{1/2}$ to account for the initial density difference (Thring and Newby 1952; Chen and Rodi 1980; Dahm and Dimotakis 1987). Turbulent transport of temperature and mass is analogous (Hinze and Van Der Hegge Zignen 1949; Chen and Rodi 1980), so that simultaneously acquired images of temperature and mole fraction provide a good mutual check on the performance of the respective diagnostics.

Figure 4 displays corresponding mixture fraction (top row) and temperature (bottom row) results for the heated jet obtained with acetone PLIF. Figure 4a, b displays typical instantaneous images of mixture fraction and temperature, while Fig. 4c presents a 100-image average. Instantaneous flow structures in the mixture fraction and temperature images are seen to be well-correlated with each other. Signal-to-noise ratio is higher for the images of acetone mole fraction than for those of temperature, as the ratio-based temperature technique is inherently less sensitive. As determined by examination of small regions in the images, single-shot rms fluctuations in mixture fraction and temperature, respectively, are 2.2% jet fluid and 8 K at the nozzle, dropping to about 1.3% jet fluid and 6 K in the freestream.

The averaged images of mixture fraction and temperature shown in Fig. 4c are in good agreement with expectation and with each other. Instantaneous images of temperature and concentration were first generated for each image pair, and 100 temperature/mole fraction image sets were then averaged. Both average temperature and average mole fraction images show a spreading angle that approaches a constant above 15 jet diameters. The half-maximum intensity points for mixture fraction and excess temperature are fit to lines extending from 16 to 21 jet diameters downstream of the nozzle to derive the virtual origin and the jet spreading rate, $dy_{0.5}/dx$ (Table 2). No trend towards higher or lower values of these parameters was apparent as the starting point of the fits was changed between 15 and 18 diameters downstream of the nozzle. Values of the spreading rate from the temperature and concentration measurements match to within experimental error; the value of 0.104 ± 0.02 obtained from the concentration image is considered more reliable. This spreading rate is within the spread of literature values, which range from 0.09 to 0.13 in other studies at

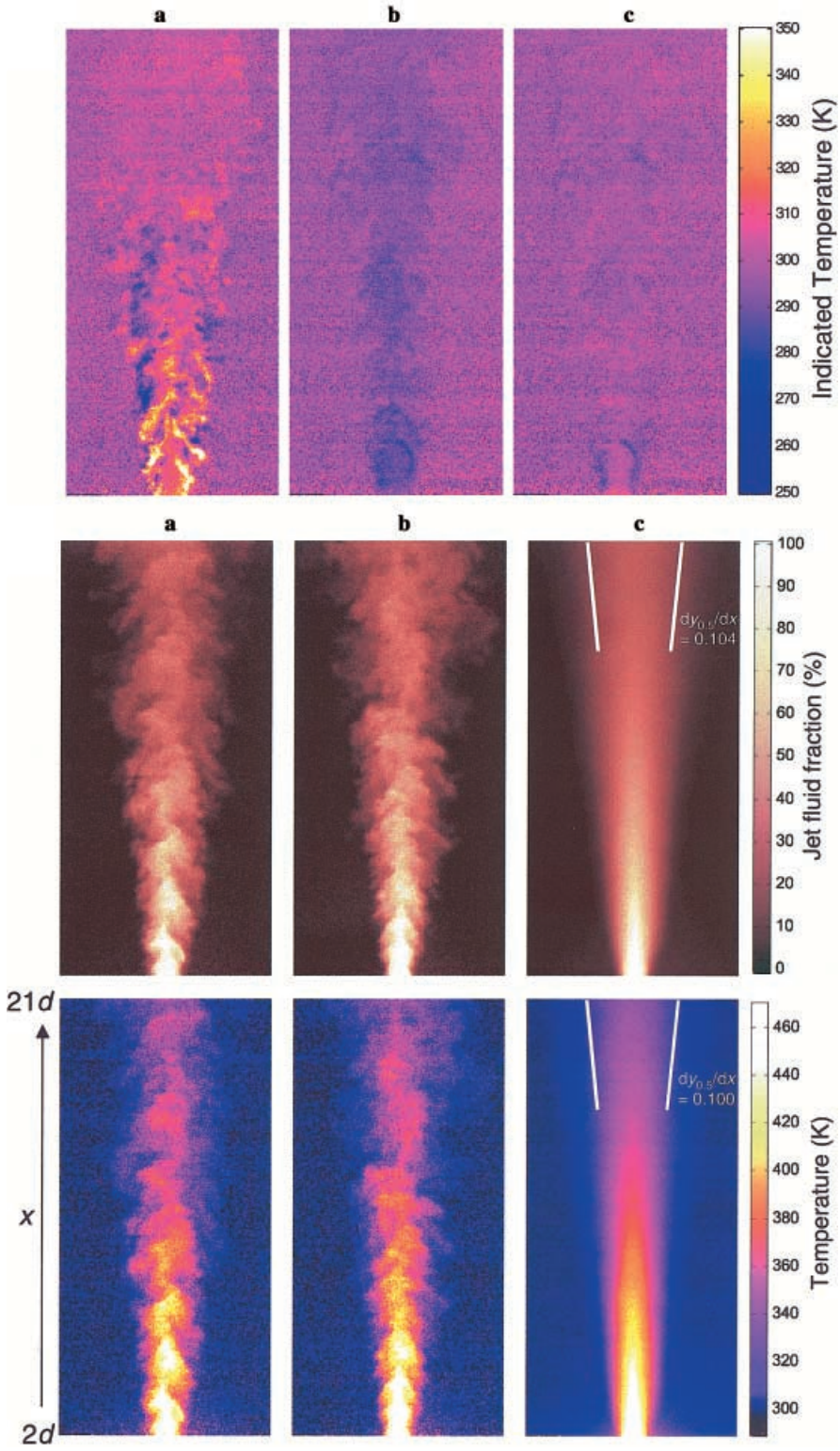

Fig. 3a–c. Images of indicated temperature for room-temperature jets: **a** mismatched sheets; **b** no correction for effect of acetone mole fraction on fluorescence yield; **c** full image correction

Fig. 4a–c. Mole fraction (*top row*) and temperature (*bottom row*) images of the heated turbulent jet (Re = 5100): **a, b** cases are representative instantaneous images; **c** 100-frame average

Table 2. Jet parameters

	Virtual origin (x/d)	Spreading rate ($dy_{0.5}/dx$)
From mole fraction	1.1 ± 0.2	0.104 ± 0.002
From temperature	1.2 ± 0.7	0.100 ± 0.007

comparable density ratios (Corrsin and Uberoi 1949; Sunavala et al. 1957; Birch et al. 1978; Lockwood and Moneib 1980; Pitts and Kashiwagi 1984).

Radial cuts of average image data in the developed jet region are expected to be Gaussian in form. In Fig. 5, both mixture fraction and temperature profiles are indeed seen to conform well to Gaussians and to each other. Data are displayed from radial, one-pixel-wide cuts through the

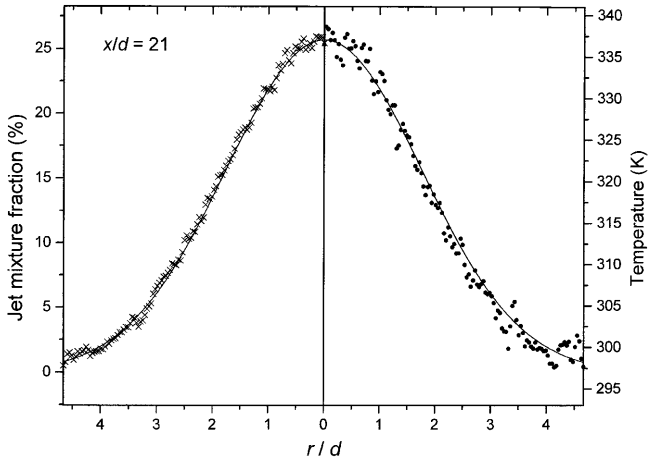

Fig. 5. Radial cuts (single-pixel rows) of average mole fraction (*left*) and average temperature (*right*) at station $x/d = 21$. The *solid lines* are Gaussian curves, with width set by the virtual origin and spreading rate from the averaged images in Fig. 4

average images of Fig. 4c at $x/d = 21$, near the tops of the images. The left half of Fig. 5 is mole fraction data, the right half temperature. The width of the Gaussian curve superimposed on the data is determined from the spreading rate and distance downstream of the virtual origin.

A final quantitative look at the PLIF image data is afforded by a cut along the centerline of the average images. Figure 6 shows the centerline decay data for both mixture fraction and excess temperature from 1 to 20 diameters downstream of the virtual origin. For the most part, temperature and mixture fraction again track each other well, although the temperature trace falls slightly above that of mixture fraction from about 3 to 8 jet diameters downstream of the virtual origin. It is suspected that this difference results from an imperfect boundary condition in temperature between jet and coflow: there is slight heating of the initial coflow immediately surrounding the jet due to the difficulty of completely insulating the jet tube and nozzle. Indeed, a rise in initial coflow temperature due to this heating is faintly visible in the temperature images of Fig. 4. As the jet becomes fully developed 15–20 diameters downstream of the virtual origin, both the mole fraction and temperature traces appear to be asymptoting to the $(x/d)^{-1}$ decay that is expected (Chen and Rodi 1980; Gouldin et al. 1986; Dowling and Dimotakis 1990).

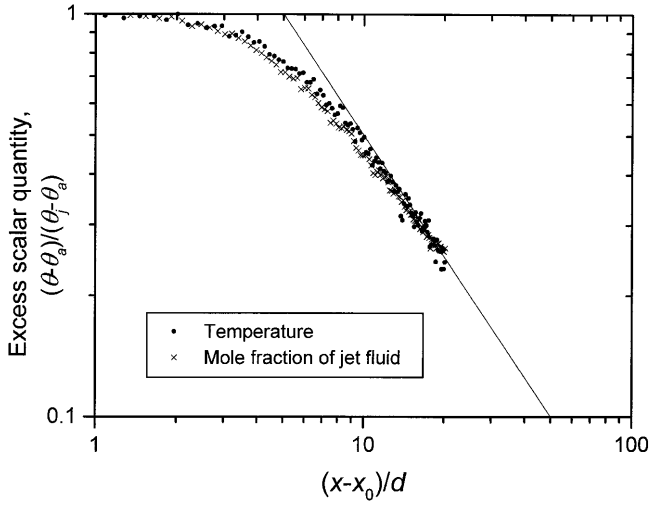

Fig. 6. Centerline cuts (single-pixel columns) from the average images of jet mixture fraction and excess temperature, plotted against number of jet diameters from the virtual origin

5 Conclusions

A heated turbulent jet experimental test case has validated the performance of a new technique for simultaneously imaging mole fraction and temperature using dual-wavelength acetone PLIF. Images with good signal-to-noise ratio can be obtained with modest experimental parameters (3%/9% coflow/jet acetone seeding, 65 mJ each in laser sheets at 248 and 308 nm, 170° C maximum temperature difference). Use of an interline transfer CCD camera allows the two required fluorescence images to be separated in time by as little as 500 ns with little increase in experimental complexity, making possible flow-stopping temporal resolution even in turbulent flows.

The appeal of the heated turbulent jet flowfield in this study is the rapid mixing, unsteadiness, and well-understood distributions of average mole fraction and temperature it provides. At the same time, this demonstration application highlights more broadly the comparative advantages of the simultaneous temperature/mole fraction imaging technique. In particular, the diagnostic is ideal for capturing instantaneous structure in flows with large temperature and mole fraction variations, especially when these variations do not coincide, as when acetone disappears through chemical reaction at higher temperatures. Even when these variations do track each other, as in the case of mixing without reaction examined here, the dual-wavelength capability is generally necessary, since highly accurate mole fraction imaging with readily available laser sources is not possible without correction of fluorescence signal for temperature variation.

References

Birch AD; Brown DR; Dodson MG; Thomas JR (1978) The turbulent concentration field of a methane jet. J Fluid Mech 88: 431–449

Bryant RA; Donbar JM; Driscoll JF (1997) Acetone LIF for flow visualization at temperatures below 300 K. AIAA Paper 97–0156

Chen CJ; Rodi W(1980) Vertical turbulent buoyant jets: a review of experimental data. Pergamon Press, Oxford

Clemens NT; Paul PH (1995) Effects of heat release on the near field flow structure of hydrogen jet diffusion flames. Combust Flame 102: 271–284

Corrsin S; Uberoi MS (1949) Further experiments on the flow and heat transfer in a heated turbulent air jet. NACA TN 1865

Dahm WJA; Dimotakis PE (1987) Measurements of entrainment and mixing in turbulent jets. AIAA J 25: 1216–1223

Dowling DR; Dimotakis PE (1990) Similarity of the concentration field of gas-phase turbulent jets. J Fluid Mech 218: 109–141

Ghandhi JB; Felton PG (1996) On the fluorescence behavior of ketones at high temperatures. Exp Fluids 21: 143–144

Gouldin FC; Schefer RW; Johnson SC; Kollmann W (1986) Nonreacting turbulent mixing flows. Prog Energy Combust. Sci 12: 257–303

Grossmann F; Monkhouse PB; Ridder M; Sick V; Wolfrum J (1996) Temperature and pressure dependences of the laser-induced fluorescence of gas-phase acetone and 3-pentanone. Appl Phys B 62: 249–253

Hinze JO; Zijnen BGVDH (1949) Transfer of heat and matter in the turbulent mixing zone of an axially symmetrical jet. Appl Sci Res A1: 435–461

Hippler H; Otto B; Troe J (1989) Collisional energy transfer of vibrationally highly excited molecules. IV. Energy dependence of $\langle \Delta E \rangle$in azulene. Ber Bunsenges Phys Chem 93: 428–434

Lockwood FC; Moneib HA (1980) Fluctuating temperature measurements in a heated round free jet. Combust Sci Tech 22: 63–81

Lozano A (1992) Laser-excited luminescent tracers for planar concentration measurements in gaseous jets. PhD dissertation, Department of Mechanical Engineering, Stanford University

Ossler F; Aldén M (1997) Measurements of picosecond laser induced fluorescence from gas phase 3-pentanone and acetone: implications to combustion diagnostics. Appl Phys B 64: 493–502

Pitts WM; Kashiwagi T (1984) The application of laser-induced Rayleigh light scattering to the study of turbulent mixing. J Fluid Mech 141: 391–429

Rossi MJ; Pladziewicz JR; Barker JR (1983) Energy-dependent energy transfer: Deactivation of azulene (S_0, E_{vib}) by 17 collider gases. J Chem Phys 78: 6695–6708

Smith SH; Mungal MG (1998) Mixing, structure and scaling of the jet in crossflow. J Fluid Mech 357: 83–122

Sunavala PD; Hulse C; Thring MW (1957) Mixing and combustion in free and enclosed turbulent jet diffusion flames. Combust Flame 1: 179–193

Tait NP; Greenhalgh DA (1992) 2D laser induced fluorescence imaging of parent fuel fraction in nonpremixed combustion. 24th Symp (Int) on Combustion, The Combustion Institute, Pittsburgh, PA, pp 1621–1628

Thring MW; Newby MP (1952) Combustion length of enclosed turbulent jet flames. Fourth Symposium (International) on Combustion. Williams & Wilkins, Baltimore, Md., pp 789–796

Thurber MC; Hanson RK (1999) Pressure and composition dependences of acetone laser-induced fluorescence with excitation at 248, 266, and 308 nm. Appl Phys B 69: 229–240

Thurber MC; Grisch F; Hanson RK (1997) Temperature imaging with single- and dual-wavelength acetone planar laser-induced fluorescence. Opt Lett 22: 251–253

Thurber MC; Grisch F; Kirby BJ; Votsmeier M; Hanson RK (1998) Measurements and modeling of acetone laser-induced fluorescence with implications for temperature-imaging diagnostics. Appl Opt 37: 4963–4978

Wolff D; Schluter H; Beushausen V; Andresen P (1993) Quantitative determination of fuel air mixture distributions in an internal combustion engine using PLIF of acetone. Ber Bunsenges Phys Chem 97: 1738–1741

Yip B; Miller MF; Lozano A; Hanson RK (1994) A combined OH/acetone planar laser-induced fluorescence imaging technique for visualized combusting flows. Exp Fluids 17: 330–336

Yuen LS; Peters JE; Lucht RP (1997) Pressure dependence of laser-induced fluorescence from acetone. Appl Opt 36: 3271–3277